Monthly Notices
of the
ROYAL ASTRONOMICAL SOCIETY

MNRAS **487,** 4856–4869 (2019)
Advance Access publication 2019 June 13

doi:10.1093/mnras/stz1643

The kiloparsec-scale gas kinematics in two star-forming galaxies at $z \sim 1.47$ seen with ALMA and VLT-SINFONI

J. Molina,[1]★ Edo Ibar,[2] I. Smail,[3] A. M. Swinbank,[3] E. Villard,[4] A. Escala,[1] D. Sobral[5] and T. M. Hughes[2,6,7,8]

[1]*Departamento de Astronomía, Universidad de Chile, Casilla 36-D, Santiago, Chile*
[2]*Instituto de Física y Astronomía, Universidad de Valparaíso, Avda. Gran Bretaña 1111, Valparaíso, Chile*
[3]*Centre for Extragalactic Astronomy, Department of Physics, Durham University, South Road, Durham DH1 3LE, UK*
[4]*Joint ALMA Observatory/ESO, Avenida Alonso de Córdova 3107, Vitacura, Santiago, Chile*
[5]*Department of Physics, Lancaster University, Lancaster LA1 4YB, UK*
[6]*CAS Key Laboratory for Research in Galaxies and Cosmology, Department of Astronomy, University of Science and Technology of China, Hefei 230026, China*
[7]*School of Astronomy and Space Science, University of Science and Technology of China, Hefei 230026, China*
[8]*Chinese Academy of Sciences South America Center for Astronomy, China-Chile Joint Center for Astronomy, Camino El Observatorio #1515, Las Condes, Santiago, Chile*

Accepted 2019 June 8. Received 2019 May 30; in original form 2019 April 3

ABSTRACT

We present Atacama Large Millimeter/submillimeter Array (ALMA) CO($J = 2$–1) observations of two main-sequence star-forming galaxies at $z \sim 1.47$ taken from the High-Z Emission Line Survey (HiZELS). These two systems have been previously reported to be molecular gas-rich $f_{\rm H_2} \equiv M_{\rm H_2}/(M_{\rm H_2} + M_\star) \sim 0.8$. We carried out a follow-up study to resolve, at ∼kpc-scales, the CO emission. These new observations are combined with our earlier ALMA observations (sensitive to diffuse CO emission) and compared with our previous Hα-based study at matched spatial resolution. One target is marginally resolved in CO(2–1), showing complex dynamics with respect to the ionized gas traced by Hα. While the other source is spatially resolved, enabling a detailed exploration of its internal dynamical properties. In this system, both gaseous phases show similar spatial extension, rotation velocities, and velocity dispersions ($V_{\rm rot} \sim \sigma_v \sim 100\,{\rm km\,s^{-1}}$) suggesting a rotational velocity to velocity dispersion ratio consistent with unity. By comparing the ionized and molecular gas tracers through the use of a two-dimensional kinematic model, we estimate a median depletion time $\tau_{\rm dep} = 2.3 \pm 1.2$ Gyr for the galaxy as a whole. This value is in agreement with the average $\tau_{\rm dep}$ value observed in local star-forming galaxies at similar spatial scales. Using a thick-disc dynamical modelling, we derive a dynamical mass $M_{\rm dyn} = (1.59 \pm 0.19) \times 10^{11}\,{\rm M_\odot}$ within ≈6 kpc. This suggests a dark matter fraction ($f_{\rm DM} \equiv M_{\rm DM}/M_{\rm dyn}$ of 0.59 ± 0.10), in agreement with the average $f_{\rm DM}$ value derived from stacked rotation curve analysis of galaxies at similar redshift range.

Key words: galaxies: evolution – galaxies: high-redshift – galaxies: ISM – galaxies: kinematics and dynamics – galaxies: star formation.

1 INTRODUCTION

Understanding how galaxies form and evolve over cosmic time is a major goal in modern astrophysics. Surveys have shown that there is a decline in the overall cosmic star formation rate (SFR) density since $z \sim 2$ (e.g. Madau et al. 1996; Sobral et al. 2013a; Khostovan et al. 2015) which coincides with the decrease of the average fraction of molecular gas mass in galaxies (e.g. Tacconi et al. 2010; Geach et al. 2012; Carilli & Walter 2013). This behaviour is thought to match the cosmic evolution of the mass in stars, and the molecular gas content ($M_{\rm H_2}$) of the Universe, hence it provides a logical interpretation for the interplay between, perhaps, the main actors controlling the growth of galaxies (e.g. Madau & Dickinson 2014).

At the peak epoch of the cosmic star formation activity ($z \sim 2$–3), spatially resolved observations of galaxies have mostly come from large *Hubble Space Telescope* (*HST*) and Integral Field Unit (IFU)

★ E-mail: juan.a.molina.t@gmail.com

surveys (e.g. Koekemoer et al. 2011; Brammer et al. 2012; Law et al. 2012b). The latter trace the ionized gas content in seeing limited conditions (∼0.″6 in *K* band, e.g. Sobral et al. 2013b; Wisnioski et al. 2015; Stott et al. 2016; Turner et al. 2017; Johnson et al. 2018). Although adaptive optics (AO)-aided IFU observations have delivered ∼0.″15 (∼kpc-scale) spatial resolution data on smaller galaxy samples (e.g. Förster Schreiber et al. 2009; Swinbank et al. 2012a; Molina et al. 2017; Förster Schreiber et al. 2018; Gillman et al. 2019). Deep observations have focused mainly in sampling the 'main sequence' of star-forming galaxies, i.e. those galaxies that are part of the bulk of the galaxy population in terms of stellar mass ($M_\star$) and SFR (e.g. Noeske et al. 2007; Whitaker et al. 2012).

High-redshift ($z \sim 1$–3) IFU surveys targeting the Hα emission have revealed that most of the main-sequence star-forming galaxies (hereafter, 'typical' star-forming galaxies), present: (1) highly turbulent galactic discs with high surface brightness, indicating that the interstellar medium (ISM) is highly pressurized with $P_{\rm tot} \sim 10^{3–4}$ times higher than the typical ISM pressure in the Milky Way (Swinbank et al. 2015; Molina et al. 2017); (2) the star formation activity is partly triggered by gravitational fragmentation of dynamically unstable gas potentially leading to the formation of massive clumps which could be up to ∼1000× more massive (∼10^9 $M_\odot$) than star-forming complexes seen in local galaxies (e.g. Genzel et al. 2011; Swinbank et al. 2012b).

Although the physical conditions that produce these extreme ISM properties remain poorly understood, one possible explanation may be related to the high molecular gas densities that may arise from the high molecular gas fractions ($f_{\rm H_2}$; e.g. Escala & Larson 2008). In the local Universe galaxies have typical $f_{\rm H_2}$ values of ∼0.1, while on the other hand galaxies at $z \sim 1$–3 have reported molecular gas fractions up to ∼0.8 (e.g. Daddi et al. 2010; Tacconi et al. 2010; Hughes et al. in preparation). The molecular gas content seems to dominate the baryonic mass budget in the central parts of these high-redshift 'typical' star-forming systems, but we have little or almost no information about their spatial distribution and kinematics.

Traditionally the workhorse tracer to estimate the molecular gas content are the low−*J* rotational transitions of the carbon monoxide ($^{12}C^{16}O$) molecule (e.g. $J = 1$–0 or $J = 2$–1; hereafter CO(1–0) and CO(2–1), respectively; Solomon & Vanden Bout 2005; Bolatto, Wolfire & Leroy 2013). Through the assumption of a CO-to-H_2 conversion factor ($\alpha_{\rm CO}$), the molecular gas to CO(1–0) luminosity ($L'_{\rm CO(1-0)}$) relation can be expressed as $M_{\rm H_2} = \alpha_{\rm CO} L'_{\rm CO(1-0)}$ (e.g. Bolatto et al. 2013). In the Milky Way and other 'normal' star-forming local galaxies, the CO emission mainly arises from individual virialized Giant Molecular Clouds (GMCs). On the other hand, the CO emission coming from more extreme star-forming and dynamically disrupted systems, such as Ultra Luminous Infrared Galaxies (ULIRGs; Downes & Solomon 1998) is likely to be contained in much denser rotating discs or rings (Solomon & Vanden Bout 2005).

Spatially resolved morphokinematic studies of the molecular gas content in galaxies are critical to understand the physical processes that control the star formation activity. Nevertheless, observations of high-redshift galaxies with direct spatially resolved molecular gas detections have remained a challenge. Beyond the local Universe, resolved CO detections are limited to the most massive/luminous yet rare galaxies or highly magnified gravitationally lensed sources (e.g. Saintonge et al. 2013; Swinbank et al. 2015; Chen et al. 2017; Calistro Rivera et al. 2018; Motta et al. 2018). With ALMA, we are now able to study the physical conditions of the cold molecular gas in 'typical' star-forming galaxies at $z > 1$ and test if the actual cosmological models successfully explain the characteristics of the high-redshift ISM.

In this paper, we use high angular resolution ALMA observations to characterize the CO(2–1) emission and kinematics of two 'typical' galaxies (following the so-called 'main sequence') at $z \sim 1.47$ drawn from the SHiZELS survey (Swinbank et al. 2012a; Molina et al. 2017; Gillman et al. 2019). Combining ALMA with the available AO-aided Hα data observed by the Spectrograph for INtegral Field Observations in the Near Infrared (SINFONI) on the Very Large Telescope (VLT), we study how the spatially resolved properties of the ionized and cold molecular gas are related on ∼kpc-scales. Throughout the paper, we adopt a ΛCDM cosmology with Ω_Λ=0.73, $\Omega_{\rm m}$=0.27, and H_0=70 km s^{-1} Mpc^{-1}, implying a spatial resolution of ≈0.″15 that corresponds to a physical scale of ∼1 kpc. We assume a Chabrier (2003) Initial Mass Function (IMF) and a Solar Oxygen abundance of 8.69 ± 0.05 in the $12+\log_{10}$(O/H) metallicity scale (Asplund et al. 2009).

2 OBSERVATIONS AND DATA REDUCTION

2.1 The SHiZELS survey

In this work, we take advantage of galaxies with previous Hα VLT-SINFONI IFU AO-aided imaging taken from the SHiZELS survey (Swinbank et al. 2012a; Molina et al. 2017; Gillman et al. 2019). This is based on a subsample of sources taken from the HiZELS near-infrared narrow-band imaging project (Sobral et al. 2012, 2013a, 2015) and is one of the largest IFU-AO survey observing the Hα emission in 'typical' star-forming galaxies on ∼kpc-scales in three narrow redshift slices $z = 0.86$, 1.47, and 2.23 ($M_\star \sim 3$–30×10^{10} $M_\odot$; SFR ∼2–30 $M_\odot$ yr^{-1}). All galaxies have a deep multiwavelength coverage as they line within the UDS, COSMOS, and SA22 fields.

From SHiZELS, we select two galaxies, COS-30 and SHiZELS-8, which have been previously detected in CO($J = 2$–1) with ALMA at ∼1.″6–2.″5 resolution (Hughes et al. in preparation).

The global stellar masses and SFRs are taken from Gillman et al. (2019). Briefly, the stellar masses were computed by using the Bayesian SED fitting code, MAGPHYS (da Cunha, Charlot & Elbaz 2008) to the rest-frame UV, optical, and near-infrared data available (*FUV*, *NUV*, *U*, *B*, *g*, *V*, *R*, *i*, *I*, *z*, *Y*, *J*, *H*, *K*, 3.6, 4.5, 5.8, and 8.0 μm collated in Sobral et al. 2014, and references therein), assuming a Chabrier (2003) IMF and a Calzetti et al. (2000) extinction law.

The SFRs are calculated from the $M_\star$-based extinction-corrected Hα emission line fluxes (Garn & Best 2010; Sobral et al. 2012; Ibar et al. 2013) and adopting the Kennicutt (1998a) calibration ${\rm SFR_{H\alpha}}$ ($M_\odot$ yr^{-1})= 4.6×10^{-42} $L_{\rm H\alpha}$ (erg s^{-1}) with a Chabrier (2003) IMF. The total Hα emission line fluxes are taken from the HiZELS narrow-band survey and are corrected for [N II] flux contamination by considering the [N II]/Hα ratio measured from the SINFONI observations. We note that the extinction-corrected SFR values presented in this work are consistent with the values reported in Gillman et al. (2019), i.e. with the intrinsic SFR values estimated by MAGPHYS. We note that the COS-30 galaxy is referred to as 'SHiZELS-19' in Gillman et al. (2019). Hereafter we use this name to refer to this galaxy.

We adopt the Whitaker et al. (2012)'s definition of the 'main sequence' of star-forming galaxies, and by using the redshift, $M_\star$ and the specific SFR (sSFR≡SFR/$M_\star$) estimates for each source, we calculate the 'distance' to the main sequence (ΔMS≡sSFR/${\rm sSFR_{MS}}(z, M_\star)$). We present the $\log_{10}$(ΔMS) values in Table 2. These values

Table 1. ALMA Cycle-5 observations. These data have been concatenated with the data shown in Hughes et al. (in preparation). 'PWV' is the average precipitable water vapour estimate for the observations.

		ALMA OBSERVATIONAL SETUP						
Source	Project ID	Observation date	Flux calibrator	Bandpass calibrator	Phase calibrator	PWV (mm)	Number of antennas	Time on target (min)
SHiZELS-8	2017.1.01674.S	2017 Nov 14	J0238+1636	J0238+1636	J0217−0820	3.17	43	47.05
		2017 Nov 15	J0238+1636	J0238+1636	J0217−0820	2.05	43	45.78
		2017 Nov 16	J0006−0623	J0006−0623	J0217−0820	1.44	43	45.82
COS-30 / SHiZELS-19	2017.1.01674.S	2017 Nov 14	J1058+0133	J1058+0133	J0948+0022	3.56	43	43.67
		2017 Nov 14	J1058+0133	J1058+0133	J0948+0022	3.92	43	44.12
		2017 Nov 16	J1058+0133	J1058+0133	J0948+0022	0.89	43	44.23
		2017 Nov 18	J1058+0133	J1058+0133	J0948+0022	0.60	43	44.50
		2017 Nov 20	J1058+0133	J1058+0133	J0948+0022	0.48	50	44.02

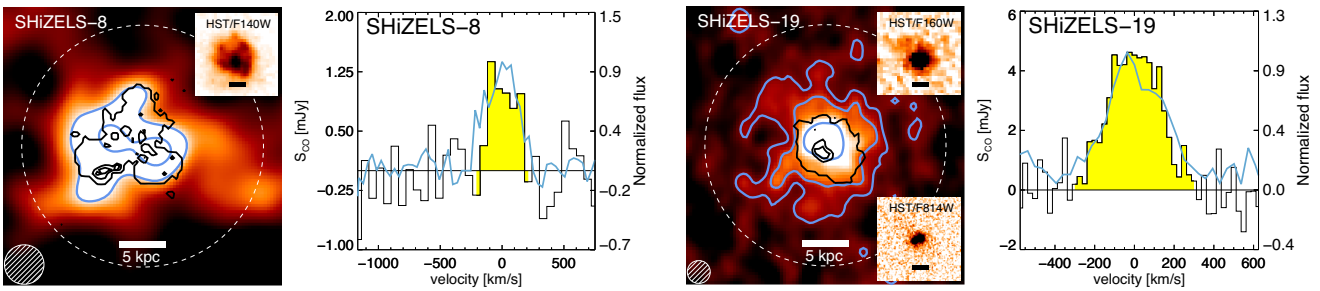

Figure 1. *First and third columns*: Spectrally integrated 2000 kλ data cubes encompassing the CO(2–1) emission line for each galaxy in a 3.″56 (≈30 kpc) squared sky region. The synthesized beam size (θ_{BMAJ} = 0.″50, 0.″29 for SHiZELS-8 and SHiZELS-19, respectively) is shown in the bottom left corner in each map. The blue contours represent the 3σ, 5σ, and 10σ levels of the image noise. The black contours show the Hα emission detected in the SINFONI-AO observations. For SHiZELS-19 we align both intensity maps by using their best-kinematic centres (see Section 3.3.1). In contrast, as we lack the detailed kinematic information for SHiZELS-8, we just align its intensity maps by eye in order to improve visualization. The dashed line represents the sky aperture defined as 2 × FWHM of the best-fit two-dimensional Gaussian in each map. If available, we also show the *HST* broad-band images over the same sky region in the right side of the map. In each *HST* cut-out, the black bar represents the 5 kpc scale. *Second and fourth columns:* Spatially collapsed spectra extracted within the sky aperture for each galaxy showing the CO(2–1) emission line. The yellow colour indicates the 2 × FWHM region for the CO emission line. The blue line shows the Hα emission line flux density normalized to the CO emission line peak and extracted from the SINFONI-AO IFU observations using the same sky aperture (Swinbank et al. 2012a; Molina et al. 2017; Gillman et al. 2019). We find good agreement between the CO and Hα line widths.

are lower than the 0.6 dex upper limit usually adopted to define the main sequence (Genzel et al. 2015).

2.2 ALMA observations and data reduction

We made use of Cycle-5 ALMA Band-3 observations (2017.1.01674.S; P.I. Molina J.; see Table 1) to detect and resolve the redshifted CO(2–1) emission line (ν_{rest} = 230.538 GHz) for SHiZELS-8 (Swinbank et al. 2012a) and SHiZELS-19 (presented as COS-30 in Molina et al. 2017). Those observations were carried during 2017 November, reaching a root-mean-squared (rms) noise of 120–150 μJy beam^{-1} at 0.″15 angular resolution using a channel width of 60 km s^{-1}.

The Cycle-5 observations were taken in an extended configuration (synthesized beam FWHM of ≈0.″15), thus being more sensitive to more compact emission. We combine them with previous 2 arcmin resolution Cycle-1 and -3 ALMA data (see Hughes et al. in preparation for more details) to obtain sensitive and high-fidelity imaging of the CO(2–1) emission.

Data were reduced using COMMON ASTRONOMY SOFTWARE APPLICATIONS[1] (CASA) considering a standard ALMA pipeline up to calibrated *u*-*v* products. We used the task TCLEAN to deconvolve the data to produce data cubes for both galaxies. In each data cube we clean the regions where emission is identified down to 3σ using the TCLEAN CASA task, allowing multiscale cleaning (MULTISCALE = [0.5,5,15,45], where image pixel size is fixed at 0.″04). The high-resolution data cubes are produced by using Briggs weighting with robust parameter at 0.5, obtaining synthesized beam FWHMs of ≈0.″15 (∼ kpc-scale at z ∼ 1.47). We also take advantage of the Cycle-1 and -3 data by producing data cubes with different spatial scales by tapering at 2000 kλ and reducing the spatial resolution using a circular restoring synthesized beam (0.″29 ≈ 2.5 kpc at z ∼ 1.47). These combined tapered data cubes are produced with the aim of recovering as much as the low surface brightness CO(2–1) emission as possible from the outskirts of each galaxy (Fig. 1).

In the case of SHiZELS-8 we are unable to detect the CO emission in the high-resolution data cube or the ≈2.5 kpc resolution map. Therefore, for this galaxy, we reduce the spectral and spatial resolutions in order to boost the CO emission signal to noise (S/N). The spectral channel width is set to 60 km s^{-1} and the spatial resolution is degraded to 0.″50 by performing an additional smoothing step.

In the case for SHiZELS-19, we are able to easily detect the source in the high-resolution data cube. Thus, for this galaxy, we set the spectral channel width to 25 km s^{-1} aiming to minimize spectral resolution effects in the derivation of the kinematic parameters.

[1] http://casa.nrao.edu/index.shtml.

Table 2. The integrated H α flux densities ($f_{H\alpha}$) are taken from narrow-band photometry and corrected for [NII] contamination. The $SFR_{H\alpha}$ values are corrected for H α extinction ($A_{H\alpha}$) following the $M_\star - A_{H\alpha}$ parametrization presented by Garn & Best (2010). ΔMS is the offset of each galaxy with respect to the 'main sequence' of star-forming galaxies. $\alpha_{CO,A+17}$ and $\alpha_{CO,N+12}$ are the CO-to-H_2 conversion values calculated by following the Accurso et al. (2017) and Narayanan et al. (2012) parametrizations. The M_{H_2} and f_{H_2} quantities are computed by using $\alpha_{CO,N+12}$ (see Section 3.4).

SPATIALLY INTEGRATED GALAXY PROPERTIES		
ID	SHiZELS-8	SHiZELS-19
RA (J2000)	02:18:21.0	09:59:11.5
Dec. (J2000)	−05:19:07.8	+02:23:24.3
z_{spec}	1.4608	1.4861
$f_{H\alpha}/10^{-17}$ (erg s^{-1} cm^{-2})	10.9 ± 1	7.6 ± 1
$A_{H\alpha}$	1.1 ± 0.2	1.1 ± 0.2
[NII]/H α	<0.1	0.43 ± 0.03
$SFR_{H\alpha}$ ($M_\odot$ yr^{-1})	16 ± 2	13 ± 2
$\log_{10}M_\star$ ($M_\odot$)	10.3 ± 0.2	10.3 ± 0.2
$\log_{10}\Delta$MS (dex)	0.53	0.41
$S_{CO(2-1)}\Delta v$ (Jy km s^{-1})	0.38 ± 0.08	0.64 ± 0.03
$\log_{10} L'_{CO(2-1)}$ (K km s^{-1} pc^2)	10.04 ± 0.04	10.27 ± 0.04
$\alpha_{CO,A+17}$ ($M_\odot$(K km s^{-1} pc^2)$^{-1}$)	21 ± 8	3.9 ± 1.5
$\alpha_{CO,N+12}$ ($M_\odot$(K km s^{-1} pc^2)$^{-1}$)	5.0 ± 1.0	1.5 ± 0.2
$\log_{10} M_{H_2}$ ($M_\odot$)	10.81 ± 0.10	10.51 ± 0.07
f_{H_2}	0.76 ± 0.24	0.62 ± 0.16

We show the spatially integrated spectrum for each galaxy in Fig. 1. Those were extracted by considering a sky aperture defined in diameter as 2 × FWHM of the best-fitting two-dimensional Gaussian in each map (∼1.″3 − 1.″2 for SHiZELS-8 and SHiZELS-19).

In summary, for SHiZELS-19 we combine Cycle-1, -3, and -5 data to generate a high-resolution (≈0.″15 ∼kpc-scale) and a 'low-resolution' (≈0.″29 ∼ 2.5 kpc) data cubes, while for SHiZELS-8 we use a ≈0.″5 resolution map (∼4.3 kpc), optimizing the flux sensitivity to the compact and diffuse emission in each source, respectively.

3 ANALYSIS, RESULTS, AND DISCUSSION

3.1 CO emission and CO-to-H_2 conversion factor

The global CO(2–1) velocity-integrated flux densities ($S_{CO(2-1)}\Delta v$) are taken from Hughes et al. (in preparation) and presented in Table 2. Those are estimated by fitting a 2D Gaussian profile to the spectrally integrated data cube (moment 0). The CO(2–1) luminosities ($L'_{CO(2-1)}$) are calculated by following Solomon & Vanden Bout (2005)

$$L'_{CO(2-1)} = 3.25\times10^7\, S_{CO(2-1)}\Delta v\, \nu_{obs}^{-2}\, D_L^2\, (1+z)^{-3}\ [\mathrm{K\,km\,s^{-1}\,pc^2}], \quad (1)$$

where $S_{CO(2-1)}\Delta v$ is in Jy km s^{-1}, ν_{obs} is the observed frequency of the emission line in GHz, D_L is the luminosity distance in Mpc, and z is the redshift. We then estimate the CO(1–0) luminosity for each galaxy by assuming a $L'_{CO(2-1)}/L'_{CO(1-0)} = 0.85$ ratio (e.g. Danielson et al. 2011).

To derive molecular gas masses we need to assume a CO-to-H_2 conversion factor. By considering a dynamical model we constrain the α_{CO} value in our galaxies (see Section 3.4). However, we also use different prescriptions in the literature to calculate tentative CO-to-H_2 conversion factor values. Unfortunately, as we lack of dust masses for SHiZELS-8 and SHiZELS-19 (see Cheng et al. in preparation), we are unable to use a dust-to-gas ratio motivated α_{CO} value (e.g. Leroy et al. 2013). Thus, from the literature we use the Accurso et al. (2017) and Narayanan et al. (2012) α_{CO} prescriptions as we have direct estimates of the input observables and these parametrizations do not require a minimum observational spatial resolution (e.g. Feldmann, Gnedin & Kravtsov 2012).

Briefly, Accurso et al. (2017)'s prescription considers the effect of the ISM metallicity and the strength of the UV radiation field in the estimation of the CO-to-H_2 conversion factor. We note that in this parametrization, the strength of the UV field is traced by the offset of the galaxy with respect to the 'main sequence' of star-forming galaxies (ΔMS; see Accurso et al. 2017, for more details). However, this prescription does not consider deviations of the α_{CO} value due to high gas surface density (Σ_{gas}) values (e.g. Bolatto et al. 2013). In contrast, the Narayanan et al. (2012)'s prescription takes into account the effect of the ISM metallicity and gas surface density in the estimation of the α_{CO} value. This is, however, a numerical prediction for Σ_{gas} and its effect is parametrized via the luminosity-weighted CO surface brightness quantity (Σ_{CO}; see Narayanan et al. 2012, for more details).

In order to apply these two α_{CO} parametrizations, we use the ΔMS values calculated by assuming the Whitaker et al. (2012)'s definition of the 'main sequence' of star-forming galaxies and presented in Table 2. The metallicities are estimated from the [N II]/H α ratio and assuming the Pettini & Pagel (2004) metallicity prescription. The inclination corrected Σ_{CO} values are calculated from the ALMA observations. Based on these assumptions, we list the global α_{CO} values for each galaxy in Table 2.

We find little agreement between the two parametrizations. By considering the Accurso et al. (2017)'s prescription, we find higher CO-to-H_2 conversion values than obtained from the Narayanan et al. (2012)'s parametrization (Table 2). This is expected as Accurso et al. (2017)'s prescription does not consider the effect of Σ_{gas} in their estimation of the α_{CO}, and it has a steeper dependence on metallicity. In the case of the Narayanan et al. (2012)'s parametrization, the low α_{CO} value obtained for SHiZELS-19 is mainly dominated by its high-galactic Σ_{CO}, which is reflected by its high-Σ_{H_2} value (Table 4). On the other hand, SHiZELS-8 has an α_{CO} value closer to that found in Galactic GMCs (Table 2). This is produced by its low (subsolar) metal content ($12+\log_{10}(O/H) < 8.12$). Although variations of the CO-to-H_2 conversion factor within galactic discs have been reported (e.g. Sandstrom et al. 2013), we note that a global α_{CO} value seems to be a good approximation for the SHiZELS-19 galaxy (Appendix A).

3.2 The SHiZELS-8 galaxy

The SHiZELS-8 H α observation (Swinbank et al. 2012a) suggests that this galaxy is consistent with being a turbulent rotating disc hosting three kpc-sized clumps (Swinbank et al. 2012b). Unfortunately the SHiZELS-8 CO(2–1) observations have too low S/N to allow a detailed dynamical characterization. This galaxy has ∼50 per cent lower velocity-integrated CO(2–1) flux density than SHiZELS-19, but its emission seems more extended, i.e. it has a lower CO surface brightness. On the other hand, our estimated low metallicity for SHiZELS-8 ($12+\log_{10}(O/H) < 8.12$) suggests a lack of dust content which could indicate an efficiently CO molecule photodissociation by the far-ultraviolet (far-UV) photons and a higher CO-to-H_2 conversion factor (Bolatto et al. 2013). This implies that SHiZELS-8 could have a larger molecular gas content than SHiZELS-19, albeit similar SFR and $M_\star$ (see Table 2).

From the high-resolution (0.″15 ∼kpc-scale) data cube we obtain a velocity-integrated peak flux density rms of 3.4 mJy km s^{-1} beam^{-1},

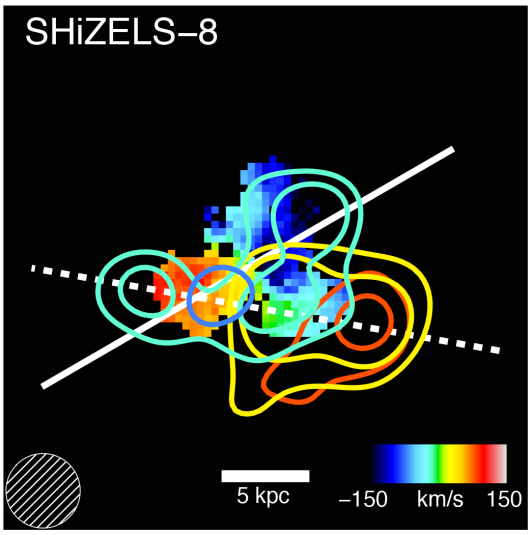

Figure 2. Hα velocity map at $\sim$kpc-scale for the SHiZELS-8 galaxy. The solid and dashed white lines represent the ionized and molecular gas major kinematic axis, respectively. The coloured contours represent the 3σ and 5σ CO(2–1) emission from the 2000 kλ tapered data cube in four spectral channels ($\Delta v = 240\,\mathrm{km\,s^{-1}}$). The synthesized beam size of this tapered observation ($\theta_{\mathrm{BMAJ}} = 0\farcs50 \sim 4.3$ kpc) is showed in the bottom left corner. We note that the apparent shift between the two maps may be produced by the astrometry inaccuracies of the SINFONI observations. Nevertheless, we note that both observations suggest that the CO(2–1) and Hα major kinematic axes are misaligned by $\sim$100–120 deg, which is indicative of a kinematic complex system.

corresponding a $\Sigma_{\mathrm{H_2}}$ upper limit of $\sim 1.6 \times 10^3\,\mathrm{M_\odot\,pc^{-2}\,beam^{-1}}$ based on the Narayanan et al. (2012)'s CO-to-H_2 conversion factor (see Section 3.4). Thus, by considering the beam angular size, we estimate a molecular gas mass 5σ upper limit of $\sim 2.8 \times 10^8\,\mathrm{M_\odot}$ to the three $\sim$kpc-scale gaseous clumps detected in the Hα observation and reported by Swinbank et al. (2012b) for this galaxy.

From the 0$\farcs$5 smoothed map we obtain a velocity-integrated peak flux density rms of 2.5 mJy km s^{-1} beam^{-1}. The lower image noise allows us to marginally detect the CO(2–1) emission in four spectral channels ($\Delta v = 240\,\mathrm{km\,s^{-1}}$). We show the SHiZELS-8 marginally detection in Fig. 2. We clearly observe the CO emission line spatial and spectral shifts produced by the internal galactic dynamics. Thus, we estimate a rough major kinematic axis position angle (PA) of $\sim$140 deg, with a peak-to-peak rotational velocity of $\sim$145 km s^{-1} (non-corrected by inclination).

3.2.1 *SHiZELS-8: a dynamically perturbed system?*

Two pieces of evidence support the idea that SHiZELS-8 is a dynamically complex system. First, the Hα and CO dynamics show that both components rotate in the same direction but have position angles offset by $\sim$100–120 deg (see Fig. 2), which is in contrast to the negligible offset in the Hα and CO dynamics seen in SHiZELS-19 (Fig. 3). Second, our previous SINFONI observation shows a flat radial [N II]/Hα metallicity gradient (Swinbank et al. 2012a).

We are possibly witnessing a massive reservoir of gas fuelling the star formation seen in Hα in a similar way to that previously seen in more violent submillimetre galaxies (SMGs; Tacconi et al. 2008). Indeed, the complex dynamics evidenced for the different ISM states

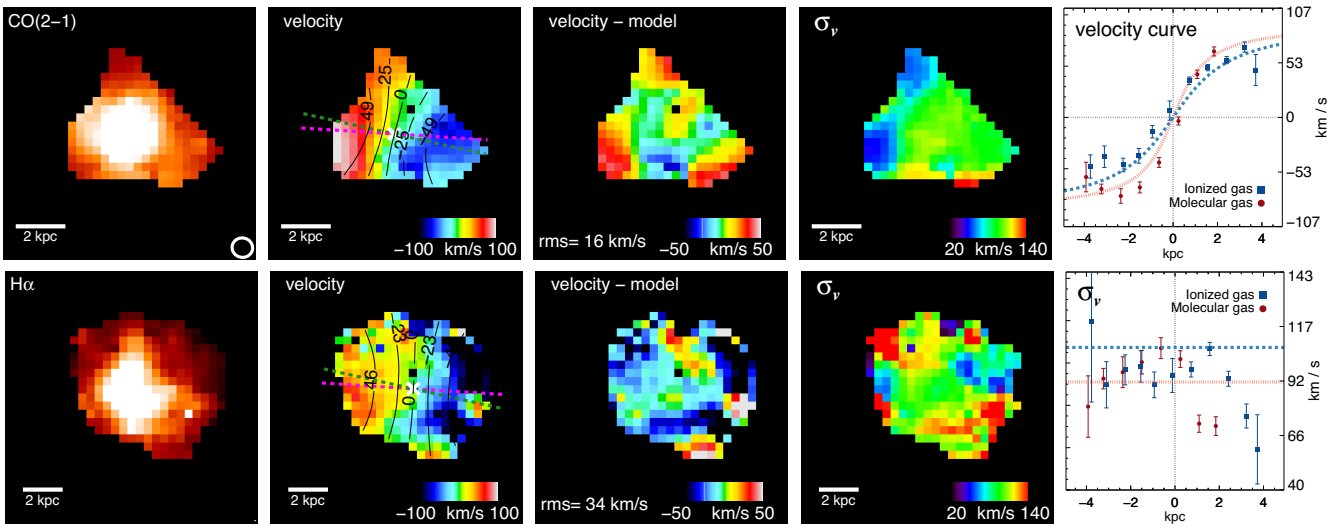

Figure 3. Intensity, velocity, residual, and velocity dispersion maps (first to fourth columns) for SHiZELS-19 obtained from CO(2–1) (top) and Hα (bottom) emission lines. In the fifth column we show the one-dimensional rotational velocity (top) and velocity dispersion (bottom) profiles across each major kinematic axis for both observations. The spatial scale for each observation is showed in each moment map. The CO(2–1) intensity map also shows the synthesized beam size. The velocity maps have overplotted the kinematic centre and the velocity contours from their best-fitting disc model. The green- and pink-dashed lines represent the molecular and ionized gas major kinematic axes, respectively. The residual fields are constructed by subtracting the velocity disc model from the velocity maps: the rms of these residuals is given in each panel. The velocity dispersion maps are corrected for beam-smearing effects. The one-dimensional profiles are constructed by using the best-fitting kinematic parameters and a slit width equal to half of the synthesized beam/PSF FWHM. In each one-dimensional profile, the error bars show the 1σ uncertainty and the vertical dashed grey line represents the best-fitting dynamical centre. In the velocity profile panel, the red- and blue-dashed curves show the velocity curve extracted from the beam-smeared CO and Hα two-dimensional best-fitting models, respectively. In the σ_v one-dimensional profile panel, the red- and blue-dashed lines show the average galactic value (Table 3) for the CO and Hα observation, respectively.

Table 3. Best-fitting kinematic parameters for SHiZELS-19 galaxy. 'inc.' is the inclination angle defined by the angle between the line of sight (LOS) and the plane perpendicular to the galaxy disc (for a face-on galaxy, inc. = 0 deg.). The velocity dispersion and half-light radii values are corrected for 'beam smearing' effects (see Section 3.3.1 for more details). The last row shows the reduced chi-squared (χ^2_ν) of the best-fitting two-dimensional model.

KINEMATIC PROPERTIES	
ID	SHiZELS-19
$PA_{H\alpha}$ (deg)	176 ± 18
$\sigma_{v,H\alpha}$ (km s^{-1})	107 ± 13
$V_{rot,H\alpha}$ (km s^{-1})	106 ± 9
$r_{1/2,H\alpha}$ (kpc)	1.80 ± 0.16
PA_{CO} (deg)	167 ± 14
$\sigma_{v,CO}$ (km s^{-1})	91 ± 6
$V_{rot,CO}$ (km s^{-1})	121 ± 10
$r_{1/2,CO}$ (kpc)	1.68 ± 0.03
inc. (deg)	27.5 ± 0.6
χ^2_ν	3.51

might be mixing the gas producing the flat metallicity gradient. We conclude that while SHiZELS-8 is a 'typical' galaxy that resides in the upper range of the 'main sequence' for star-forming galaxies, which follows the Kennicutt–Schmidt law (see Hughes et al. in preparation), it is probably experiencing torques that will eventually drive a flow of gas into the central regions. The SHiZELS-8 case demonstrates the wide variety of galaxy kinematics within the 'main sequence' (Elbaz et al. 2018). Given the impossibility to describe this source as a virialized rotating disc, in the remaining of this work we focus on the analysis of the SHiZELS-19 galaxy.

3.3 The SHiZELS-19 galaxy

We derive the two-dimensional intensity and kinematic maps for SHiZELS-19 by analysing the CO(2–1) emission line following the approach presented in Swinbank et al. (2012a). Briefly, we spatially bin the ALMA data cube up to a scale given by the synthesized beam and then we perform an emission line fitting approach using a χ^2 minimization procedure (see Swinbank et al. 2012a, for more details). In each iteration a Gaussian profile is fitted in the frequency domain to estimate the intensity, velocity, and velocity dispersion information (Fig. 3). We highlight that for this galaxy, the Hα emission line properties were derived and presented in an analogous manner in Molina et al. (2017).

We show the CO(2–1) intensity, velocity, and line-of-sight velocity dispersion maps for SHiZELS-19 in Fig. 3, whilst the best-fitting kinematic parameters are listed in Table 3. We observe a smooth CO(2–1) intensity map with no apparent clumpiness, which is consistent with the morphology observed in the Hα intensity map (Molina et al. 2017) and the *HST* F160W-band (rest-frame optical) image. However, this galaxy presents an irregular morphology in the *HST* F814W-band map (rest-frame UV, Fig. 1). The discrepancy between the galaxy morphology seen in the *HST* images suggests that the irregular morphology seen in the *HST* F814W-band image may just reflect a complex dust distribution through the galactic disc (e.g. Genzel et al. 2013).

3.3.1 Global dynamical properties

In order to characterize the dynamical properties of SHiZELS-19, we fit the two-dimensional velocity fields for the ionized and molecular gas jointly. We construct two-dimensional models with an input rotation curve following an arctan function [$V(r) = \frac{2}{\pi} V_{asym} \arctan(r/r_t)$], where V_{asym} is the asymptotic rotational velocity and r_t is the effective radius at which the rotation curve turns over (Courteau 1997). We consider the 'disc thickness' by modelling the galaxy as an oblate spheroid system with intrinsic minor-to-major axis ratio of 0.2, a value that seems appropriate for the high-redshift galaxy population (Law et al. 2012a). As the CO and Hα velocity fields are consistent (Fig. 3), we also model both velocity fields by coupling the inclination angle parameter. We do not attempt to lock the dynamical centres through RA−DEC coordinates as the SINFONI astrometry is not accurate enough to allow it, nevertheless we are assuming that the ionized and molecular gas ISM phases are coplanar. We also allow the possibility that their rotational motions can be out of phase, i.e. both ISM phases could have different kinematic PA.

This modelling has 11 free parameters ($V_{asym,H\alpha}$, $r_{t,H\alpha}$, $PA_{H\alpha}$, $[x/y]_{H\alpha}$, $V_{asym,CO}$, $r_{t,CO}$, PA_{CO}, $[x/y]_{CO}$, and inclination angle; see Table 3) and a genetic algorithm (Charbonneau 1995) is used to find the best-fitting model (see Swinbank et al. 2012a for more details). The total χ^2 of the model is calculated as the sum of the χ^2 obtained from each two-dimensional modelled map.

In Molina et al. (2017) the kinematic model for SHiZELS-19 was performed without any constraint on the inclination angle value. This adds an additional source of uncertainty as the inclination angle is poorly constrained from the velocity field modelling alone (Glazebrook 2013). In order to deal with this uncertainty, we constrain the inclination angle by fitting a two-dimensional Sérsic model (Sérsic 1963) to the CO intensity map (moment 0) using GALFIT (Peng et al. 2010). We obtain an observed minor-to-major axis ratio of ∼0.90 ± 0.05, which corresponds to an inclination angle value of ∼26 ± 6 deg. However, as GALFIT tends to underestimate the parameter errors, we consider a more conservative inclination angle uncertainty of ±10 per cent in our fitting procedure (Epinat et al. 2012).

We use the dynamical centres and position angles derived from the best-fitting dynamical models to extract the one-dimensional rotation curve and velocity dispersion profile across the major kinematic axes of the ionized and molecular gas. The extracted one-dimensional rotational curves and dispersion velocity profiles are presented in Fig. 3.

We calculate the half-light radius ($r_{1/2}$) for each ISM component by following Molina et al. (2017), and we define the rotational velocity for the ionized and molecular gas component ($V_{rot,H\alpha}$, $V_{rot,CO}$) as the inclination-corrected velocity observed at two times the Hα and CO half-light radii, respectively (see Table 3).

Even at the ∼kpc-scales achieved here, there is still a contribution to the derived line widths from the beam-smeared large-scale velocity motions across the galaxy (Davies et al. 2011). In order to correct for these effects, we calculate the velocity gradients ($\Delta V/\Delta R$) across the synthesized beam and point spread function (PSF) in the CO and Hα velocity field models, respectively. We subtract them linearly from the corresponding velocity dispersion map by following equation (A1) from Stott et al. (2016). However, by using this procedure, ∼20 per cent residuals are expected to remain, especially at the centres of each galaxy map where large velocity gradients are expected to be present (Stott et al. 2016). In order to minimize such effects, we define the global velocity dispersion for each gas phase ($\sigma_{v,CO}$, $\sigma_{v,H\alpha}$) as the median value taken from the pixels beyond the central galactic zone. This zone is defined as three times the size of the angular resolution of the map.

The best-fitting kinematic maps and velocity residuals for the Hα and CO derived maps are shown in Fig. 3. The best-fitting inclination, PA, and half-light radius values are given in Table 3. The mean deviation from the best-fitting model (indicated by the typical rms) is given in each residual map.

The molecular and ionized gas components show similar scale sizes $r_{1/2,\mathrm{H}\alpha}/r_{1/2,\mathrm{CO}} \approx 1.07 \pm 0.09$. We stress that the CO and Hα analyses are obtained from images created at matched spatial resolution (0.″15; corresponding to ∼kpc-scale at $z \sim 1.47$). Possible loss of the extended CO flux in the high-resolution observation may reduce the $r_{1/2,\mathrm{CO}}$ value in our calculation. Nevertheless, our estimation of the half-light radius for both ISM components are slightly smaller than the half-light radius value measured from the *HST* F160W-band image $r_{1/2,\mathrm{HST\text{-}F160W}} = 2.1 \pm 0.5$ kpc (Gillman et al. 2019).

The CO(2–1) velocity map shows a clear rotational pattern, roughly matching the rotational motions traced by the ionized gas component. From the two-dimensional modelling, we find that the kinematic position angles agree ($\Delta\mathrm{PA} \equiv \mathrm{PA_{H\alpha}} - \mathrm{PA_{CO}} = 9 \pm 23$ deg) within the 1σ error range. The velocity curves roughly agree, except in the blueshifted zone where the CO traced rotation curve drops to lower velocity values. However, we note that the ionized gas velocity map is noisier than the molecular gas velocity map, especially in the galaxy outskirts. This may be partly produced by OH line features present in the *H*−band spectra, whilst the ALMA observation is free from sky-line residuals. We find that, the ionized gas component shows a slightly lower rotational velocity value when compared to that from the molecular gas observations ($V_{\mathrm{rot,H}\alpha}/V_{\mathrm{rot,CO}} \approx 0.88 \pm 0.10$). This might be due to differences in the spatial distribution between the two ISM components.

In terms of velocity dispersion, the CO observation shows a slightly lower average velocity dispersion value than the mean value observed from the ionized gas component ($\sigma_{v,\mathrm{H}\alpha}/\sigma_{v,\mathrm{CO}} \approx 1.18 \pm 0.16$). The difference between the ALMA (25 km s^{-1}) and *H*−band SINFONI (50 km s^{-1}) spectral resolutions should not produce such differences as the intrinsic CO and Hα line widths are significantly broader. The high-σ_v values observed at the outskirts of the Hα velocity dispersion map may increase the ionized gas average value. In a similar way as the comparison between the velocity maps, the ionized gas velocity dispersion map is noisier than the molecular gas map at larger radii. By considering all the pixels in the mean σ_v estimation, we obtain an average $\sigma_{v,\mathrm{H}\alpha}$ value of 91 ± 13 km s^{-1} (Molina et al. 2017), in agreement with the measured $\sigma_{v,\mathrm{CO}}$ value (Table 3). Thus, we suggest that both ISM tracers show similar supersonic turbulence values.

We derive rotational velocity to dispersion velocity ratio ($V_{\mathrm{rot}}/\sigma_v$) values of 0.99 ± 0.14 and 1.33 ± 0.14 for the ionized and molecular gas ISM phases, respectively. This suggests that the disordered motions of both ISM phases are playing an important role in the galactic support against self-gravity (Burkert et al. 2010).

3.3.2 *Kinematic asymmetry characterization*

In order to obtain a detailed characterization of the ionized and molecular gas kinematics, we quantify the kinematic deviations from the ideal rotating disc case by performing a '*kinemetry*' analysis (Krajnović et al. 2006). Briefly, *kinemetry* proceeds to analyse the two-dimensional kinematic maps using azimuthal profiles in an outward series of best-fitting tilted rings. The kinematic profile as a function of angle is then expanded harmonically, which is equivalent to a Fourier transformation which has coefficients $k_{n,v}$ and $k_{n,\sigma}$ at each tilted ring for the velocity and velocity dispersion maps, respectively. In the velocity map, the first-order decomposition '$k_{1,v}$' is equivalent to the rotational velocity value, and therefore, the ideal rotating disc case is simply described by the cosine law along the tilted rings ($V(\theta) = k_{1,v}\cos(\theta)$). The high-order terms describe the kinematic anomalies with respect to the ideal rotating disc case (see Krajnović et al. 2006 for more details). We note that *kinemetry* stops the radial fitting when there are less than 75 per cent of the pixels sampled along the best-fitting tilted ring (Krajnović et al. 2006).

We restrict the inclination and position angles within the 1σ error range given by our best-fitting two-dimensional model. The $k_{n,v}$ and $k_{n,\sigma}$ errors are derived by bootstrapping via Monte Carlo simulations the errors in measured velocities, velocity dispersions, and estimated dynamical parameters.

We quantify the kinematic deviations from the ideal disc case by computing three different estimators used in the literature: (1) the $k_{5,v}/k_{1,v}$ ratio (Krajnović et al. 2006); (2) the $(k_{2,v} + k_{3,v} + k_{4,v} + k_{5,v})/4k_{1,v}$ and $(k_{1,\sigma} + k_{2,\sigma} + k_{3,\sigma} + k_{4,\sigma} + k_{5,\sigma})/5k_{1,}v$ fractions (Shapiro et al. 2008); and (3) the $(k_{3,v} + k_{5,v})/2k_{1,v}$ and $(k_{2,\sigma} + k_{4,\sigma})/2k_{1,v}$ ratios (Bloom et al. 2018). The first case is the traditional dimensionless ratio that describes the kinematic asymmetries just in the velocity map. It does not consider the low-order coefficients as these are used by '*kinemetry*' to find the best-fitting tilted rings at a given radius (Krajnović et al. 2006). The second case was defined to classify galaxy mergers which tend to present extremely disturbed kinematic fields (Shapiro et al. 2008). The third case consists on a slight modification to the second case as it takes into account that in moderately disturbed systems, the even/odd moments contribution measured from the velocity/velocity dispersion maps are negligible (Bloom et al. 2018).

In Fig. 4 we show the different estimators of the kinematic deviations for the CO and H α velocity and velocity dispersion maps as a function of the deprojected radius. We note that the shorter CO radial profiles compared to the Hα radial profiles are produced by the stop of the 'kinemetry' procedure at shorter radius due to the lack of roundness of the CO two-dimensional maps derived from our observations.

In the case of the velocity map, the $k_{5,v}/k_{1,v}$ (Krajnović et al. 2006) ratio gives lower values along the galactic disc compared with the other two estimators. We obtain an average $k_{5,v}/k_{1,v}$ ratio of 0.04 ± 0.01 and 0.09 ± 0.05 for the CO and Hα velocity map, respectively. This difference is mainly produced by the higher $k_{5,v}/k_{1,v}$ values found in the Hα velocity map at longer radius ($\gtrsim$ 2 kpc). This gradient suggests that SHiZELS-19 suffered a merger event in the past as the outer regions retain better the kinematic perturbations by remaining out of equilibrium while the central region tends to relax faster to a disc-like system (Kronberger et al. 2007).

If we follow the kinematic classification performed to the ATLAS^{3D} (Krajnović et al. 2011) and SAMI local galaxy surveys (van de Sande et al. 2017) and we consider their $k_{5,v}/k_{1,v} = 0.04$ limit value to classify systems as regular rotators, this would imply that SHiZELS-19 corresponds to a 'non-regular' rotator, i.e. the velocity field presents significant kinematic deviations that make it not well described by the cosine law.

In the case of the velocity dispersion map, we found that the Bloom et al. (2018)'s estimator is higher than the Shapiro et al. (2008)'s estimator at all radii. The additional $k_{n,\sigma}$ coefficients considered in the latter case contribute little to the kinematic asymmetry estimator. This may also suggests that SHiZELS-19 is a moderate disturbed system. We also note that, as a difference

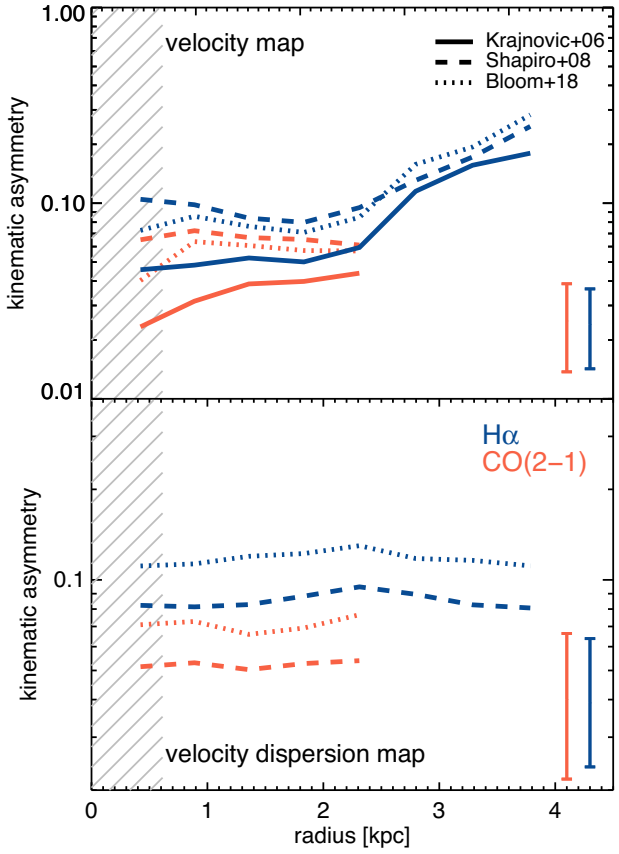

Figure 4. Kinematic asymmetry radial profiles measured from the SHiZELS-19 velocity (*top*) and velocity dispersion (*bottom*) maps. We plot the CO(2–1) and Hα observations. The line, dashed line, and dotted line represent the kinematic asymmetry estimators presented in Krajnović et al. (2006), Shapiro et al. (2008), and Bloom et al. (2018) for each map (see Section 3.3.2 for more details). The colour-coded error bars show the median 1σ uncertainties in each panel. The grey-dashed area represents the resolution element radial extent. Despite of the estimator used, the ionized gas two-dimensional maps tend to show slightly higher kinematic deviations from the ideal rotating disc case than the molecular gas kinematic maps. Although, the measurements agree within 1σ error range.

from the velocity map, the kinematic asymmetries in the CO and Hα velocity dispersion map tend to be nearly constant along the galactic disc. The kinematic deviations measured from the CO velocity dispersion map tend to be lower than the ones measured from the Hα velocity map, however, they agree between the 1σ error range.

The rough agreement between the molecular and ionized gas kinematics suggests that, at ∼kpc-scales, both phases of the ISM are tracing the galactic dynamics instead of peculiar kinematics (e.g. gas inflows/outflows). This is in agreement with previous studies of massive galaxies (at ∼0.4 to 2.4 $\times$ 10^{11} $M_{\odot}$) at similar redshift (e.g. Calistro Rivera et al. 2018; Übler et al. 2018).

3.4 Dynamical mass and dark matter content

The dynamical mass estimate is a useful tool that allows us to measure the total galactic mass enclosed as a function of radius. It provides a simple way to probe the existence of dark matter haloes (e.g. Gnerucci et al. 2011) or to constrain the CO-to-H_2 conversion factor (e.g. Calistro Rivera et al. 2018; Motta et al. 2018).

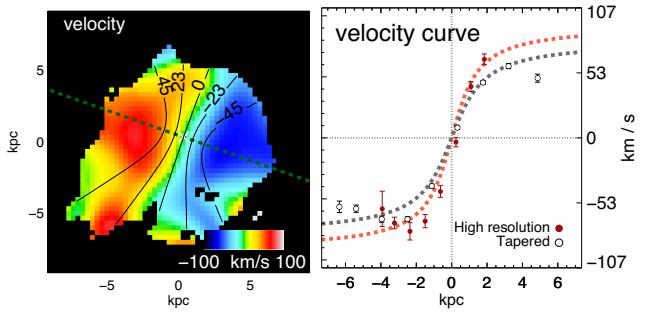

Figure 5. Velocity map, and velocity profile for the CO(2–1) 2000 kλ tapered data cube for SHiZELS-19. We use the same colour coding presented in Fig. 3. In this case, the one-dimensional velocity profile is constructed by using the best-fitting kinematic parameters for the tapered data cube and a slit width equal to half of the tapered synthesized beam FWHM. We also overplot the data taken from the ∼kpc-scale high-resolution observations. The tapered rotation curve extends up to ≈6 kpc.

By measuring the global kinematics of a galaxy, the dynamical mass can be easily estimated from the rotational velocity (e.g. Genzel et al. 2011) considering a thin-disc dynamical mass approximation ($M_{\rm dyn,thin}$). On the other hand, if the supersonic turbulence across the galactic disc is comparable to the ordered motions amplitude, then, an additional pressure gradient support contribution against self-gravity has to be considered. In this limit, the galactic disc height is not negligible and a thick-disc approximation ($M_{\rm dyn,thick}$) should be considered (Burkert et al. 2010).

We calculate the dynamical mass for the SHiZELS-19 galaxy by using the kinematic information from our CO observations as its velocity map shows lower kinematic asymmetry amplitudes compared to the Hα velocity map (Section 3.3.2). Since the CO ∼kpc-scale observations are more sensitive to the denser and compact emission, we use a tapered version (2000 kλ) of the ALMA observations that allows us to trace the diffuse and more extended CO emission (at 0.″29 resolution). This allows us to observe a rotation curve up to a radial distance of ≈6 kpc or ∼3.5 times the CO half-light radius (Fig. 5).

Taking into account that the Sérsic index derived from the *HST* image is consistent with unity for this galaxy (Gillman et al. 2019), we assume an exponential disc surface density profile. This implies that, in terms of the disc scale length ($r_{\rm d}$), we observe the rotation curve up to ≈6$r_{\rm d}$ ($r_{1/2}$ ≈ 1.67$r_{\rm d}$ for an exponential disc).

By using the inclination-corrected rotational velocity value derived from the tapered rotation curve at radius of ≈6 kpc ($V_{\rm rot,tap}$ = 112 ± 6 km s^{-1}), we would obtain a total enclosed mass of $M_{\rm dyn,thin}(r \lesssim 6\,{\rm kpc}) = (1.75 \pm 0.19) \times 10^{10}\,{\rm M}_{\odot}$ assuming a thin-disc approximation. This dynamical mass estimate is lower but consistent within 1σ range with the estimated stellar mass for this galaxy scaled at the same radius ($M_{\star}(r \lesssim 6\,{\rm kpc}) \approx 0.98 M_{\star} \approx (1.96 \pm 0.90) \times 10^{10}\,{\rm M}_{\odot}$). However, this 'thin-disc' dynamical mass value would suggest that this galaxy has almost no gaseous mass content, evidencing an apparent discrepancy with our CO and Hα emission line measurements. On the other hand, as the $V_{\rm rot}/\sigma_v$ ratio is consistent with unity for both ISM components, this suggests that the $M_{\rm dyn,thin}$ quantity may be underestimating the total mass of this galaxy. Additional support against self-gravity needs to be considered.

We follow the analysis by Burkert et al. (2010), and we consider a possible additional pressure support by calculating the dynamical mass in the thick-disc approximation. In the 'thick-disc' dynamical

mass modelling, the radial pressure gradient term in the hydrostatic equation cannot be neglected and it is parametrized by the galactic velocity dispersion and the mass density distributions. This approximation further assumes that σ_v is independent of the galaxy disc radius and height. We use Burkert et al. (2010)'s equation (11) with $\sigma_{v,\mathrm{CO}}$ and $r_{1/2,\mathrm{CO}}$ as input values and we obtain $M_{\mathrm{dyn,thick}} = (1.59 \pm 0.19) \times 10^{11}\,\mathrm{M}_\odot$. This dynamical mass value is ∼8 times higher than $M_\star$, erasing any discrepancy between both quantities, but allowing the possibility of a non-negligible amount of dark matter content in this galaxy.

In order to test this, we calculate the dark matter fraction by comparing the total mass budget from our dynamical analysis with the luminosity-based total mass content. We consider the total $M_\star$ value estimated for the SHiZELS-19 galaxy as its difference with the scaled value at 6 kpc ($M_\star - M_\star(r \lesssim 6\,\mathrm{kpc}) \approx 0.02 M_\star$) is negligible compared to the stellar mass uncertainty (see Table 2). Therefore, by considering the $M_\star$, $M_{\mathrm{H_2}}$, and M_{dyn} quantities, we define the dark matter fraction as

$$f_{\mathrm{DM}} \equiv 1 - \frac{M_\star + M_{\mathrm{H_2}}}{M_{\mathrm{dyn,thick}}} = 1 - \frac{\alpha_{\mathrm{CO}} L'_{\mathrm{CO}} + M_\star}{M_{\mathrm{dyn,thick}}}, \quad (2)$$

where the molecular mass content is estimated via the CO luminosity ($M_{\mathrm{H_2}} = \alpha_{\mathrm{CO}} L'_{\mathrm{CO}}$). However, this mass sum approach needs additional information about the CO-to-$\mathrm{H_2}$ conversion factor in order to overcome the degeneracy between α_{CO} and f_{DM}. We also note that strong dependence on the assumptions behind $M_\star$, M_{dyn}, and L'_{CO} may also affect the result from equation (2).

Thus, in order to properly consider the $M_\star$, M_{dyn}, and L'_{CO} uncertainties and the degeneracy between α_{CO} and f_{DM}, we reproduce the parameter space built up in equation (2) by applying an MCMC technique following Calistro Rivera et al. (2018). Briefly, based on the likelihood of the measured L'_{CO}, $M_\star$, and M_{dyn} values, we sample the posterior probability density function (posterior PDF) for α_{CO} and f_{DM} parameters using the EMCEE algorithm (Foreman-Mackey et al. 2013).

We note that SED fitting techniques based on unresolved flux observations may lead to the underestimation of the galactic stellar mass values (Sorba & Sawicki 2018). Thus, we consider an additional case in which we assume that the stellar mass content is being underestimated by a factor of two. This is likely to be an extreme case as suggested by Sorba & Sawicki (2018) for galaxies with similar sSFR.

In Fig. 6 we show the one- and two-dimensional posterior PDFs of the α_{CO} and f_{DM} parameters. We also show the CO-to-$\mathrm{H_2}$ conversion factor values suggested by following Accurso et al. (2017) and Narayanan et al. (2012). From the two-dimensional posterior PDF we observe the strong degeneracy between both parameters regardless of the $M_\star$ value assumed. Lower α_{CO} values imply higher dark matter fractions. We note that if we assume the Accurso et al. (2017)'s α_{CO} value, we obtain $f_{\mathrm{DM}} \sim 0.3 \pm 0.13$. Although SHiZELS-19 has a metallicity consistent with being solar, its ISM morphology and kinematics departs strongly from the ISM conditions observed in local galaxies. The high molecular gas velocity dispersion values (Table 3) observed for this system suggest that SHiZELS-19 should have a dense ISM (Papadopoulos et al. 2012) which may lower its CO-to-$\mathrm{H_2}$ conversion factor value (Bolatto et al. 2013). As the Accurso et al. (2017)'s parametrization does not consider the ISM density effects, its α_{CO} value should be considered as an upper limit. This is also consistent with the α_{CO} upper limit derived from the dynamical mass estimate within the CO half-light radius (see Appendix B, for more details.). Thus, in the remaining of this work, we use the Narayanan et al. (2012)'s

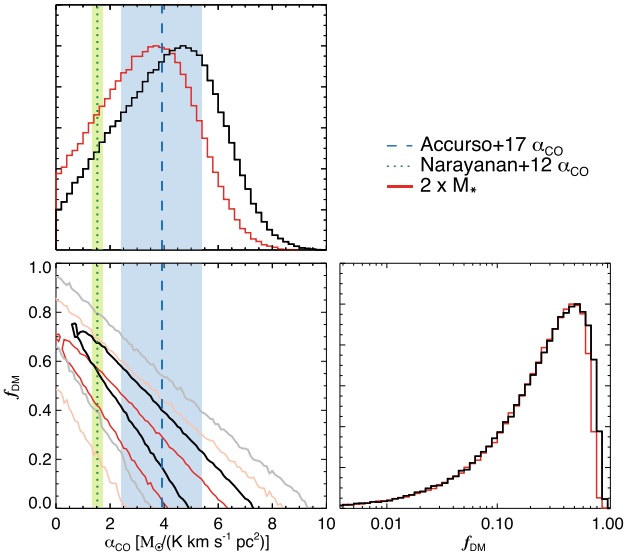

Figure 6. One- and two-dimensional posterior PDFs of the f_{DM} and α_{CO} parameters for SHiZELS-19. The one-dimensional PDFs are represented by the black line in the *top left-hand* and *bottom right-hand* panels. The red line represents the inference assuming 2× the stellar mass value derived from the spatially unresolved SED fitting, thus we consider a possible underestimation of $M_\star$ as suggested from spatially resolved studies (Sorba & Sawicki 2018). In *bottom left*-hand panel we show the two-dimensional PDFs, i.e. the covariance between both parameters. The black and grey lines show the 1σ and 3σ regions of the PDF derived by using the stellar mass value obtained from the spatially unresolved SED fitting. The red and orange lines show the 1σ and 3σ regions by assuming a stellar mass correction factor of two. In the *bottom* and *top left*-hand panels, the dashed and dotted lines show the CO-to-$\mathrm{H_2}$ conversion factors calculated by following the Accurso et al. (2017) and Narayanan et al. (2012) parametrizations, respectively. The blue- and green-shaded regions show the 1σ uncertainties for each parametrization.

parametrization as it does consider the ISM density effect in the estimation of α_{CO}.

We find $f_{\mathrm{DM}} \approx 0.59 \pm 0.10$ for SHiZELS-19. This value is consistent with the dark matter fraction predicted for disc-like galaxies at similar redshift range and stellar mass content from hydrodynamical simulations (Lovell et al. 2018). From our Bayesian approach, we find 3σ range boundaries of ∼0.31–0.70 for the f_{DM} value. On the other hand, if we consider the extreme case of a stellar mass underestimated by a factor of two (Sorba & Sawicki 2018), then the 3σ range boundaries correspond to ∼0.20–0.64.

To determine if we need to include the H I content in our analysis, we note that in local spirals the transition between a $\mathrm{H_2}$- to HI-dominated ISM ($\Sigma_{\mathrm{H_2}} \approx \Sigma_{\mathrm{HI}}$) occurs at a gas surface density of $\Sigma_{\mathrm{gas}} \sim 12 \pm 6\,\mathrm{M_\odot\,pc^{-2}}$ (Leroy et al. 2008). In contrast, from our spatially resolved CO(2–1) observations, we derive an average $\Sigma_{\mathrm{H_2}} \sim 220 \pm 166\,\mathrm{M_\odot\,pc^{-2}}$ value from a tilted ring centred at the same radius at which $V_{\mathrm{rot,tap}}$ was calculated. This suggests that the HI mass content within a radius of ≈6 kpc is likely to be negligible compared to $M_{\mathrm{H_2}}$ and therefore, our estimated f_{DM} value may be a good approximation. Thus, we suggest that SHiZELS-19 is a 'typical' star-forming galaxy which may have a considerable dark matter content.

The dark matter fraction obtained for SHiZELS-19 is consistent with the values reported by Tiley et al. (2019), but in tension with the conclusions reported from Genzel et al. (2017) and Lang et al. (2017). These three studies rely primarily on the analysis of

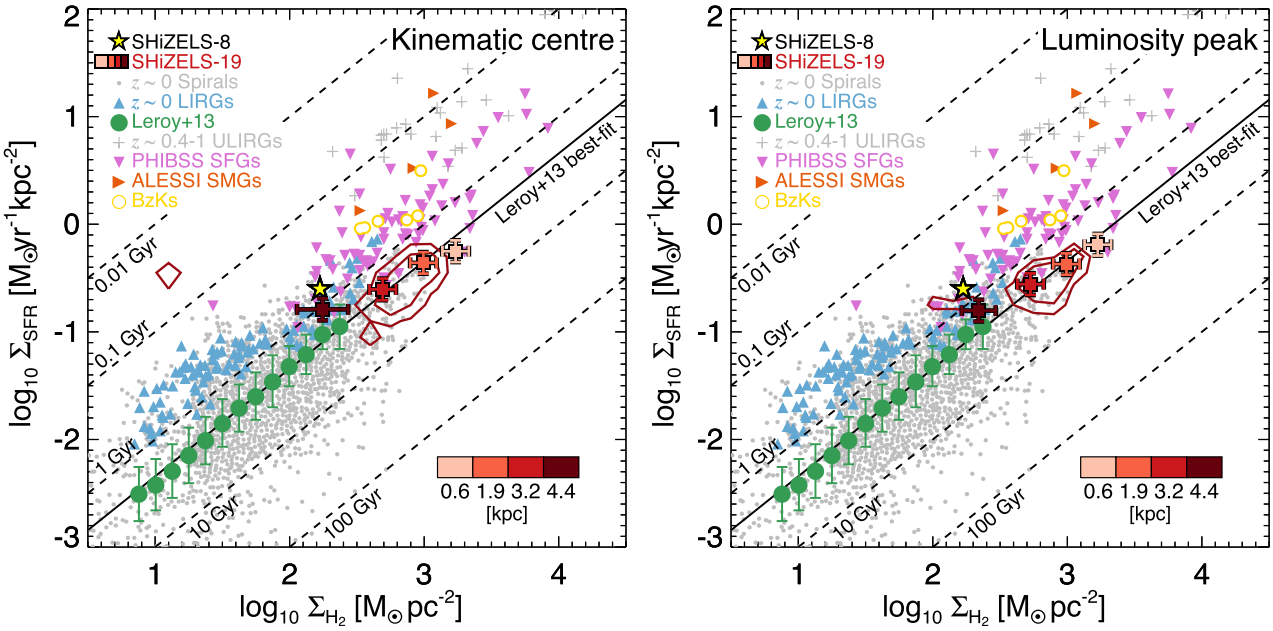

Figure 7. *Left:* Σ_{SFR} against Σ_{H_2} for SHiZELS-8 and SHiZELS-19 galaxies compared with spatially resolved local galaxy observations in the literature. For SHiZELS-8 we just show a global estimate given the limitations of our marginally detected CO observation. For SHiZELS-19 we centre the CO(2–1) and Hα two-dimensional intensity maps by using the best-fitting kinematic centre. The red contours show the 50th and 90th percentile levels of the pixel-by-pixel distribution. The colour-coded squares represent the Σ_{SFR}–Σ_{H_2} values calculated within tilted rings of 0.″15 (∼1.2 kpc) thickness at the radius indicated by the colour bar. The '$z \sim 0$ Spirals' sample consist in observations of local discs taken from Kennicutt et al. (2007), Blanc et al. (2009), and Rahman et al. (2011, 2012) at spatial resolutions between ∼0.2–1 kpc. The '$z \sim 0$ LIRGs' values consist in ∼1 kpc scale observations of two galaxies (Espada et al. 2018). The green circles show the median trend observed in the HERACLES survey (Leroy et al. 2013) at ∼kpc-scales and the black line represents the best fit for those median values. The error bars represent the 1σ uncertainty. We also present galaxy-integrated estimates of ULIRGs ($z \sim 0.4$–1; Combes et al. 2013), four SMGs taken from the ALESS survey ($z \sim 2.0$–2.9; Calistro Rivera et al. 2018), 'typical' star-forming galaxies observed at similar redshifts (Tacconi et al. 2013) and five *BzK* galaxies ($z \sim 1.5$; Daddi et al. 2010). The dashed lines indicate fixed τ_{dep} values. *Right:* The same plot as shown in the left-hand panel, but now the CO(2–1) and Hα two-dimensional intensity maps are centred by using the CO and Hα luminosity peaks.

the stacked rotation curve constructed from normalized individual velocity curves from galaxies in the $0.6 \lesssim z \lesssim 2.6$ redshift range. However, the discrepancy between the obtained f_{DM} values from these studies seems to be driven by the way in which the velocity curves are normalized. In Genzel et al. (2017) and Lang et al. (2017) works they normalize the individual velocity curves in both, radial extension through the turn-over radius and velocity amplitude through the velocity at the turn-over radius (see Lang et al. 2017 for more details). This normalization procedure tends to favour the contribution of the systems with low-V_{rot}/σ_v values to the stacked rotation curve at longer radii. This bias seems to be produced by the smaller turn over radius values presented in those galaxies which acts as a 'zoom-in' scaling factor (Tiley et al. 2019). On the other hand, Tiley et al. (2019) normalize the individual velocity curves by the stellar light disc-scale radius and also velocity. In this case, galaxies with different V_{rot}/σ_v values contribute more uniformly to the shape of the stacked rotation curve. Taking this into account, we note that SHiZELS-19 is a galaxy with $V_{rot}/\sigma_v \sim$ 1.0–1.3, favouring the scenario in which the conclusions presented in Genzel et al. (2017) and Lang et al. (2017) studies may be biased.

3.5 The Kennicutt–Schmidt law at ∼kpc-scales

First proposed by Schmidt (1959) and extended by Kennicutt (1998a,b), the Kennicutt–Schmidt law is an observational power-law relationship between the galaxy SFR surface density (Σ_{SFR}) and the gas surface density. It describes how efficiently galaxies turn their gas content into stars. For local galaxies, this correlation is well fitted by an exponent of $N = 1.4$ (Kennicutt 1998b).

Since then, latter studies have found that Σ_{SFR} is better correlated with the molecular gas surface density (Σ_{H_2}) rather than Σ_{gas} (e.g. Bigiel et al. 2008; Leroy et al. 2008). At first order, local disc-like galaxies show a linear correlation between both surface density quantities ($\Sigma_{SFR} \propto \Sigma_{H_2}$), with a median depletion time ($\tau_{dep} \equiv \Sigma_{H_2}/\Sigma_{SFR}$) of ∼2.2 Gyr (e.g. Leroy et al. 2013). Second-order departures from this relationship have also been found (e.g. Saintonge et al. 2012; Utreras, Becerra & Escala 2016), although these effects may be related to systematic errors behind the estimation of the molecular gas content and/or local nuclear starburst activity (Leroy et al. 2013).

In Fig. 7 we present the star formation activity of SHiZELS-8 and SHiZELS-19 in the context of the Σ_{SFR}–Σ_{H_2} relation. We compare with several local galaxy samples observed at similar spatial scales and galactic averages of galaxies observed at similar redshifts. Briefly, the '$z \sim 0$ spirals' sample is composed by high spatial resolution (∼0.2–1 kpc) observations of small galactic regions taken from Kennicutt et al. (2007), Blanc et al. (2009), and Rahman et al. (2011, 2012). The '$z \sim 0$ LIRGs' sample consist in observations of the NGC3110 and NGC232 galaxies observed at ∼1 kpc scale (Espada et al. 2018). Both starburst systems have SFR∼20 $M_\odot$ yr^{-1}, i.e. comparable with the value reported for SHiZELS-19 (SFR = 23 $M_\odot$ yr^{-1}). NGC3110 is a barred Sb galaxy interacting with a minor companion (mass ratio ∼14:1), while NGC232 corresponds to a barred Sa galaxy which presents a bright compact nuclear region (see Espada et al. 2018, for more

details). We also compare with the median trend observed for a subsample of 30 local galaxies taken from the HERA CO Line Extragalactic Survey (HERACLES; Leroy et al. 2013). These data also consist in ∼1 kpc scale observations of the galactic ISM. The high-redshift observations consist in galaxy-integrated estimates from ULIRGs ($z \sim 0.4$–1; Combes et al. 2013), four SMGs taken from the ALESS survey ($z \sim 2.0$–2.9; Calistro Rivera et al. 2018), 'typical' star-forming galaxies observed at $z \sim 1$–2.5 taken from the PHIBSS survey (Tacconi et al. 2013) and five *BzK* galaxies ($z \sim 1.5$) presented in Daddi et al. (2010). For the ALESS SMGs we calculate the surface density quantities following Tacconi et al. (2013).

Given our marginally detected CO observation for SHiZELS-8, we just plot a galactic average estimation ($\log_{10}\Sigma_{\rm SFR} \approx -0.61 \pm 0.07\,{\rm M}_\odot\,{\rm yr}^{-1}\,{\rm kpc}^{-2}$; $\Sigma_{\rm H_2} \sim 2.23 \pm 0.08\,{\rm M}_\odot\,{\rm pc}^{-2}$). However, we caution that in this particular case, $\Sigma_{\rm H_2}$ is a rough estimation as we cannot constrain the SHiZELS-8's CO spatial distribution accurately. For SHiZELS-19, we use the interactive data language (IDL) procedure HASTROM to align the two-dimensional fields using as a reference point the kinematic centre (left-hand panel) and the luminosity peak position (right-hand panel) from Hα and CO ∼kpc-scale observations. For this galaxy, we derive a median $\log_{10}\Sigma_{\rm SFR} = -0.5 \pm 0.3\,{\rm M}_\odot\,{\rm yr}^{-1}\,{\rm kpc}^{-2}$ and $\log_{10}\Sigma_{\rm H_2} = 3.0 \pm 0.6\,{\rm M}_\odot\,{\rm pc}^{-2}$ values. These estimations indicate that SHiZELS-19 has a somewhat denser ISM compared with local star-forming galaxies. On the other hand, the median $\Sigma_{\rm H_2}$ value is consistent with molecular surface density estimations from galaxy-integrated observations of *BzK* and 'typical' star-forming galaxies at similar redshifts (Daddi et al. 2010; Tacconi et al. 2013), but SHiZELS-19 presents lower $\Sigma_{\rm SFR}$ values compared to these systems.

We derive a median $\tau_{\rm dep} = 2.3 \pm 1.2$ Gyr for this galaxy, with the pixel-by-pixel distribution between ∼0.003–5 Gyr. SHiZELS-19 presents a median depletion time consistent with the best-fitting $\tau_{\rm dep} = 2.2 \pm 0.28$ Gyr reported in Leroy et al. (2013) for the median trend observed in local galaxies at similar spatial resolution.

In the left-hand panel of Fig. 7 we show the $\tau_{\rm dep}$ values calculated from tilted rings constructed from the two-dimensional best-fitting model and centred at the kinematic centre. At first order, we find the same trend suggested from the average $\tau_{\rm dep}$ values. But, at second order, we note that the depletion times vary from $\sim 1.0 \pm 0.3$ Gyr in the outer ring (≈4.4 kpc) to $\sim 2.9 \pm 0.2$ Gyr in the central kpc of this galaxy, suggesting an apparent decrease in the star formation efficiency (SFE$\equiv \tau_{\rm dep}^{-1}$) towards the galactic centre in SHiZELS-19. This is in contradiction with second-order effects found in galaxies in the local Universe. Possible variations of the CO-to-H_2 conversion factor through a radial dependence of the dust-to-gas ratio optical depth or gas excitation or nuclear starburst activity in galactic centres favour the opposite $\tau_{\rm dep}$ correlation with galactic radius (e.g. Leroy et al. 2013; Sandstrom et al. 2013). However, by using the [N II/Hα] ratio as a proxy of the metallicity gradient (Pettini & Pagel 2004), we find a $\alpha_{\rm CO}$ radial profile consistent with being flat (see Appendix A).

On the other hand, although the CO and Hα maps are smooth, the Hα best-fitting kinematic centre does not coincide exactly with the Hα luminosity peak as it does in the CO observations. Indeed, the projected distance between both centres is ∼0.″11, i.e. slightly lower than the spatial resolution of the observations (≈0.″15). Thus, possible inaccuracies of our best-fitting kinematic centres given by the limited spatial resolution of our observations may lead to the apparent outward decrease of the $\tau_{\rm dep}$ values obtained from the tilted rings. In order to explore this possibility, in the right-hand panel of Fig. 7 we show the $\tau_{\rm dep}$ values calculated from tilted rings constructed from the two-dimensional best-fitting model but centred at the luminosity peak. For this case, the $\tau_{\rm dep}$ values vary from $\sim 1.3 \pm 0.3$ Gyr in the outer ring to $\sim 2.5 \pm 0.1$ in the inner ring. The increase of the $\tau_{\rm dep}$ values towards the galactic centre still remains.

Table 4. Summary of the SHiZELS-19 galaxy parameters derived in this work using the kinematic modelling. The $f_{\rm DM}$, $\Sigma_{\rm H_2}$, and $\tau_{\rm dep}$ values are computed by considering the Narayanan et al. (2012)'s CO-to-H_2 conversion factor (see Section 3.4).

SHiZELS-19 FINAL PARAMETERS	
$f_{\rm DM}$	0.59 ± 0.10
$\log_{10}\Sigma_{\rm SFR}$ (${\rm M}_\odot\,{\rm kpc}^{-2}$)	-0.5 ± 0.3
$\log_{10}\Sigma_{\rm H_2}$ (${\rm M}_\odot\,{\rm pc}^{-2}$)	3.0 ± 0.6
$\tau_{\rm dep}$ (Gyr)	2.3 ± 1.2

The suppression of the star formation in the molecular gas by dynamical effects is a possibility. For example, a morphological quenching scenario in which the bulge stabilizes the molecular gas, preventing the star formation activity but not destroying the gas may explain the observed $\tau_{\rm dep}$ trend with galactocentric radius (e.g. Martig et al. 2009; Saintonge et al. 2011). However, this scenario is unlikely as the Sérsic index measured for SHiZELS-19 ($n \sim 1$; Gillman et al. 2019) indicates that this galaxy is consistent with being a disc-like galaxy with no prominent bulge component. Galaxies with a prominent bulge component tend to show Sérsic index values deviated from unity (Lang et al. 2014). On the other hand, Schreiber et al. (2016) found that the increase of $\tau_{\rm dep}$ towards the central galactic zone in massive systems ($M_\star \sim 10^{11}\,{\rm M}_\odot$) seems to be independent of the possible mass growth of the bulge component as disc-dominated galaxies tend to present the same $\tau_{\rm dep}$ trend with radius.

Another possible effect that adds uncertainty to the calculated $\tau_{\rm dep}$ values is a potential spatial variation of the Hα extinction. We have used an $A_{\rm H\alpha}$ correction constant across the galactic disc, but an underestimated galactic extinction in the galactic centre may lower the observed $\tau_{\rm dep}$ values in the central kpc zone therefore, producing the observed trend. An increase of the Hα extinction towards the galactic centre is consistent with findings of $A_{\rm H\alpha}$ being correlated with stellar mass surface density (Hemmati et al. 2015) or the presence of compact density starbursts (e.g. Simpson et al. 2015; Hodge et al. 2016, 2018).

In order to explore the effects of the global galaxy kinematics in the global star formation activity, we compute the orbital time-scale ($\tau_{\rm orb} = 2\pi R/V_{\rm rot}$) to be compared it with the median depletion time-scale (e.g. Kennicutt 1998b; Daddi et al. 2010). By following the analysis of Daddi et al. (2010), we choose R to be equal to three times the half-light radius. Although this assumes that the rotation curve remains flat beyond two half-light radius (the radius at which $V_{\rm rot}$ was estimated), this seems to be a reasonable assumption (see Fig. 5 and Tiley et al. 2019). Thus, we obtain $\tau_{\rm orb} = 256 \pm 22$ Myr and $\tau_{\rm dep}/\tau_{\rm orb} \sim 9 \pm 5$. We find that SHiZELS-19 converts ∼10 per cent of its available gas into stars per orbit. This is consistent with the average value found for local galaxies by Kennicutt (1998b) and with galaxy-integrated studies of *BzK* galaxies at similar redshifts (Daddi et al. 2010). Therefore, on average, SHiZELS-19 is a galaxy which follows a similar star formation law to that seen in local spiral galaxies, although in denser environments.

We should stress, however, that our conclusions are highly dependent on the assumed $\alpha_{\rm CO}$ value (Table 4) and its variation with radius. We have used the CO-to-H_2 conversion suggested by Narayanan et al. (2012) in order to consider possible variations in the average ISM metallicity and density (see also Appendix A).

However, spatially resolved observations of the dust content are desirable as these may help to constrain the α_{CO} value through a dust-to-gas-to ratio based approach (Leroy et al. 2013; Sandstrom et al. 2013).

Our work opens the possibility to perform morphokinematic analysis of high-redshift galaxies at ∼kpc-scales using two different ISM tracers, but we stress that more observations of 'typical' galaxies are needed to understand the impact of local or global galactic properties on the star formation activity in high-redshift systems.

4 CONCLUSIONS

We present new ALMA Cycle-5 observations tracing the CO(2–1) emission line from two 'typical' star-forming galaxies at $z \sim 1.47$. These observations were designed to deliver spatially resolved observations of the molecular gas content on ∼kpc-scales. We combine our ALMA observations with the previous Hα SINFONI AO-aided observations (Swinbank et al. 2012a; Molina et al. 2017; Gillman et al. 2019) in order to study and compare the ionized and molecular gas dynamics.

One of our targets, SHiZELS-8, is marginally detected only in the 2000kλ tapered data cube (0.″5 ∼ 4.3 kpc spatial resolution). For this system the Hα and CO dynamics show that both ISM components rotate in the same direction but have position angles offset by 100–120 deg. This suggests that SHiZELS-8 is a dynamically perturbed system consistent with its previously observed flat metallicity gradient (Swinbank et al. 2012a). This finding suggests that 'main-sequence' galaxies at high redshift are not exclusively part of a well-behaved morphokinematic disc-like population (e.g. Elbaz et al. 2018).

For the other target, SHiZELS-19, we find a good agreement between the CO and Hα spatial extent ($r_{1/2,H\alpha}/r_{1/2,CO} \sim 1.07 \pm 0.09$) and dynamics at ∼kpc-scales (Fig. 3). From both ISM phases we derive $V_{rot}/\sigma_v \sim 1$ (Table 3). By performing a kinemetry analysis we classify SHiZELS-19 as a 'non-regular rotator' (van de Sande et al. 2017). The kinematic analysis suggests that the CO and Hα observations are tracing the same galactic kinematics in agreement with previous studies of massive galaxies at similar redshift range (e.g. Calistro Rivera et al. 2018; Übler et al. 2018).

We estimate the total mass budget of the SHiZELS-19 galaxy by assuming a galactic thick-disc geometry (Burkert et al. 2010) and Narayanan et al. (2012)'s CO-to-H_2 conversion factor. From the SHiZELS-19 2000kλ data cube we are able to trace the CO emission up to ≈6 kpc (Fig. 5), finding a dark matter fraction of $f_{DM} = 0.59 \pm 0.10$ within this aperture. By applying an MCMC technique to sample the posterior PDF and take into account the parameter uncertainties (Fig. 6; e.g. Calistro Rivera et al. 2018) we estimate a f_{DM} 3σ error range of ∼0.31–0.70. The dark matter fraction value is in agreement with hydrodynamical simulations of disc-like galaxies with similar stellar mass (Lovell et al. 2018) and the average dark matter fraction suggested by the stacked rotation curve analysis of galaxies at similar redshift range (Tiley et al. 2019). Thus, we conclude that SHiZELS-19 is a 'typical' star-forming galaxy at $z \sim 1.47$ harbour in a non-negligible amount of dark matter.

By using two-dimensional modelling, we study the star formation activity observed in the SHiZELS-19 galaxy at ∼kpc-scales. We derive a median $\tau_{dep} = 2.3 \pm 1.2$ Gyr. This median value is consistent with the typical value observed in local galaxies at similar spatial scales ($\tau_{dep} = 2.2 \pm 0.28$ Gyr; Leroy et al. 2013) and consistent with the large scatter presented in the $z \sim 0$ spirals galaxy observations (Fig. 7), suggesting that 'typical' high-redshift galaxies (at $z \sim 1.47$) with denser ISM still follow the same star formation law.

ACKNOWLEDGEMENTS

We thank to the anonymous referee for her/his careful read of the manuscript and helpful comments and suggestions. J.M. acknowledges the support given by CONICYT Chile (CONICYT-PCHA/Doctorado-Nacional/2014-21140483).
E.I. acknowledges partial support from FONDECYT through grant N° 1171710. A.E. acknowledges support from CONICYT project Basal AFB-170002 and Proyecto Regular FONDECYT (grant 1181663). I.R.S. and A.M.S. acknowledge the support from STFC (ST/P000541/1). This paper makes use of the following ALMA data: ADS/JAO.ALMA#2018.1.01740.S, ADS/JAO.ALMA#2012.1.00402.S and ADS/JAO.ALMA#2015.1.00862.S. ALMA is a partnership of ESO (representing its member states), NSF (USA) and NINS (Japan), together with NRC (Canada), NSC and ASIAA (Taiwan), and KASI (Republic of Korea), in cooperation with the Republic of Chile. The Joint ALMA Observatory is operated by ESO, AUI/NRAO, and NAOJ.

REFERENCES

Accurso G. et al., 2017, MNRAS, 470, 4750
Asplund M., Grevesse N., Sauval A. J., Scott P., 2009, ARA&A, 47, 481
Bigiel F., Leroy A., Walter F., Brinks E., de Blok W. J. G., Madore B., Thornley M. D., 2008, AJ, 136, 2846
Blanc G. A., Heiderman A., Gebhardt K., Evans Neal J. I., Adams J., 2009, ApJ, 704, 842
Bloom J. V. et al., 2018, MNRAS, 476, 2339
Bolatto A. D., Wolfire M., Leroy A. K., 2013, ARA&A, 51, 207
Brammer G. B. et al., 2012, ApJS, 200, 13
Burkert A. et al., 2010, ApJ, 725, 2324
Calistro Rivera G. et al., 2018, ApJ, 863, 56
Calzetti D., Armus L., Bohlin R. C., Kinney A. L., Koornneef J., Storchi-Bergmann T., 2000, ApJ, 533, 682
Carilli C. L., Walter F., 2013, ARA&A, 51, 105
Chabrier G., 2003, PASP, 115, 763
Charbonneau P., 1995, ApJS, 101, 309
Chen C.-C. et al., 2017, ApJ, 846, 108
Combes F., García-Burillo S., Braine J., Schinnerer E., Walter F., Colina L., 2013, A&A, 550, A41
Courteau S., 1997, AJ, 114, 2402
da Cunha E., Charlot S., Elbaz D., 2008, MNRAS, 388, 1595
Daddi E. et al., 2010, ApJ, 713, 686
Danielson A. L. R. et al., 2011, MNRAS, 410, 1687
Davies R. et al., 2011, ApJ, 741, 69
Dekel A., Burkert A., 2014, MNRAS, 438, 1870
Downes D., Solomon P. M., 1998, ApJ, 507, 615
Elbaz D. et al., 2018, A&A, 616, A110
Epinat B. et al., 2012, A&A, 539, A92
Escala A., Larson R. B., 2008, ApJ, 685, L31
Espada D. et al., 2018, ApJ, 866, 77
Feldmann R., Gnedin N. Y., Kravtsov A. V., 2012, ApJ, 747, 124
Foreman-Mackey D., Hogg D. W., Lang D., Goodman J., 2013, PASP, 125, 306
Förster Schreiber N. M. et al., 2009, ApJ, 706, 1364
Förster Schreiber N. M. et al., 2018, ApJS, 238, 21
Garn T., Best P. N., 2010, MNRAS, 409, 421
Geach J. E., Sobral D., Hickox R. C., Wake D. A., Smail I., Best P. N., Baugh C. M., Stott J. P., 2012, MNRAS, 426, 679
Genzel R. et al., 2011, ApJ, 733, 101
Genzel R. et al., 2013, ApJ, 773, 68

Genzel R. et al., 2015, ApJ, 800, 20
Genzel R. et al., 2017, Nature, 543, 397
Gillman S. et al., 2019, MNRAS, 486, 175
Glazebrook K., 2013, Publ. Astron. Soc. Aust., 30, e056
Gnerucci A. et al., 2011, A&A, 528, A88
Hemmati S., Mobasher B., Darvish B., Nayyeri H., Sobral D., Miller S., 2015, ApJ, 814, 46
Hodge J. A. et al., 2016, ApJ, 833, 103
Hodge J. A. et al., 2018, ApJ, 876, 130()
Ibar E. et al., 2013, MNRAS, 434, 3218
Johnson H. L. et al., 2018, MNRAS, 474, 5076
Kennicutt R. C., Jr, 1998a, ARA&A, 36, 189
Kennicutt Robert C. J., 1998b, ApJ, 498, 541
Kennicutt Robert C. J. et al., 2007, ApJ, 671, 333
Khostovan A. A., Sobral D., Mobasher B., Best P. N., Smail I., Stott J. P., Hemmati S., Nayyeri H., 2015, MNRAS, 452, 3948
Koekemoer A. M. et al., 2011, ApJS, 197, 36
Krajnović D., Cappellari M., de Zeeuw P. T., Copin Y., 2006, MNRAS, 366, 787
Krajnović D. et al., 2011, MNRAS, 414, 2923
Kronberger T., Kapferer W., Schindler S., Ziegler B. L., 2007, A&A, 473, 761
Lang P. et al., 2014, ApJ, 788, 11
Lang P. et al., 2017, ApJ, 840, 92
Law D. R., Steidel C. C., Shapley A. E., Nagy S. R., Reddy N. A., Erb D. K., 2012a, ApJ, 745, 85
Law D. R., Steidel C. C., Shapley A. E., Nagy S. R., Reddy N. A., Erb D. K., 2012b, ApJ, 745, 85
Leroy A. K., Walter F., Brinks E., Bigiel F., de Blok W. J. G., Madore B., Thornley M. D., 2008, AJ, 136, 2782
Leroy A. K. et al., 2013, AJ, 146, 19
Lovell M. R. et al., 2018, MNRAS, 481, 1950
Madau P., Dickinson M., 2014, ARA&A, 52, 415
Madau P., Ferguson H. C., Dickinson M. E., Giavalisco M., Steidel C. C., Fruchter A., 1996, MNRAS, 283, 1388
Martig M., Bournaud F., Teyssier R., Dekel A., 2009, ApJ, 707, 250
Molina J., Ibar E., Swinbank A. M., Sobral D., Best P. N., Smail I., Escala A., Cirasuolo M., 2017, MNRAS, 466, 892
Motta V. et al., 2018, ApJ, 863, L16
Narayanan D., Krumholz M. R., Ostriker E. C., Hernquist L., 2012, MNRAS, 421, 3127
Noeske K. G. et al., 2007, ApJ, 660, L43
Papadopoulos P. P., van der Werf P., Xilouris E., Isaak K. G., Gao Y., 2012, ApJ, 751, 10
Peng C. Y., Ho L. C., Impey C. D., Rix H.-W., 2010, AJ, 139, 2097
Pettini M., Pagel B. E. J., 2004, MNRAS, 348, L59
Queyrel J. et al., 2012, A&A, 539, A93
Rahman N. et al., 2011, ApJ, 730, 72
Rahman N. et al., 2012, ApJ, 745, 183
Saintonge A. et al., 2011, MNRAS, 415, 61
Saintonge A. et al., 2012, ApJ, 758, 73
Saintonge A. et al., 2013, ApJ, 778, 2
Sandstrom K. M. et al., 2013, ApJ, 777, 5
Schmidt M., 1959, ApJ, 129, 243
Schreiber C., Elbaz D., Pannella M., Ciesla L., Wang T., Koekemoer A., Rafelski M., Daddi E., 2016, A&A, 589, A35
Sérsic J. L., 1963, BAAA, 6, 41
Shapiro K. L. et al., 2008, ApJ, 682, 231
Simpson J. M. et al., 2015, ApJ, 799, 81
Sobral D., Best P. N., Matsuda Y., Smail I., Geach J. E., Cirasuolo M., 2012, MNRAS, 420, 1926
Sobral D., Smail I., Best P. N., Geach J. E., Matsuda Y., Stott J. P., Cirasuolo M., Kurk J., 2013a, MNRAS, 428, 1128
Sobral D. et al., 2013b, ApJ, 779, 139
Sobral D., Best P. N., Smail I., Mobasher B., Stott J., Nisbet D., 2014, MNRAS, 437, 3516
Sobral D. et al., 2015, MNRAS, 451, 2303
Solomon P. M., Vanden Bout P. A., 2005, ARA&A, 43, 677
Sorba R., Sawicki M., 2018, MNRAS, 476, 1532
Stott J. P. et al., 2016, MNRAS, 457, 1888
Swinbank A. M., Sobral D., Smail I., Geach J. E., Best P. N., McCarthy I. G., Crain R. A., Theuns T., 2012a, MNRAS, 426, 935
Swinbank A. M., Smail I., Sobral D., Theuns T., Best P. N., Geach J. E., 2012b, ApJ, 760, 130
Swinbank A. M. et al., 2015, ApJ, 806, L17
Tacconi L. J. et al., 2008, ApJ, 680, 246
Tacconi L. J. et al., 2010, Nature, 463, 781
Tacconi L. J. et al., 2013, ApJ, 768, 74
Tiley A. L. et al., 2019, MNRAS, 485, 934
Turner O. J. et al., 2017, MNRAS, 471, 1280
Utreras J., Becerra F., Escala A., 2016, ApJ, 833, 13
van de Sande J. et al., 2017, ApJ, 835, 104
Whitaker K. E., van Dokkum P. G., Brammer G., Franx M., 2012, ApJ, 754, L29
Wisnioski E. et al., 2015, ApJ, 799, 209
Zolotov A. et al., 2015, MNRAS, 450, 2327
Übler H. et al., 2018, ApJ, 854, L24

APPENDIX A: α_{CO} RADIAL PROFILE

Throughout this work we have used a simple CO-to-H_2 conversion factor to estimate the molecular gas content in SHiZELS-8 and SHiZELS-19 galaxies (Section 3.1). Thus, we have assumed that there is no significant radial variation of the α_{CO} value across each galactic disc. In order to test this assumption, we calculate the CO-to-H_2 conversion factor radial profile. This can only be done for the SHiZELS-19 galaxy since we were not able to obtain spatially resolved CO observations for SHiZELS-8. In Fig. A1 we show the α_{CO} as a function of the galactocentric radius. It was calculated by using the Narayanan et al. (2012)'s parametrization with the CO surface brightness radial profile and metallicity gradient as input values. We find an α_{CO} gradient consistent with being flat. This is mainly produced by the sublinear dependence of the CO-to-H_2 conversion factor with respect to Σ_{CO} and metallicity in the Narayanan et al. (2012)'s parametrization. Although SHiZELS-19

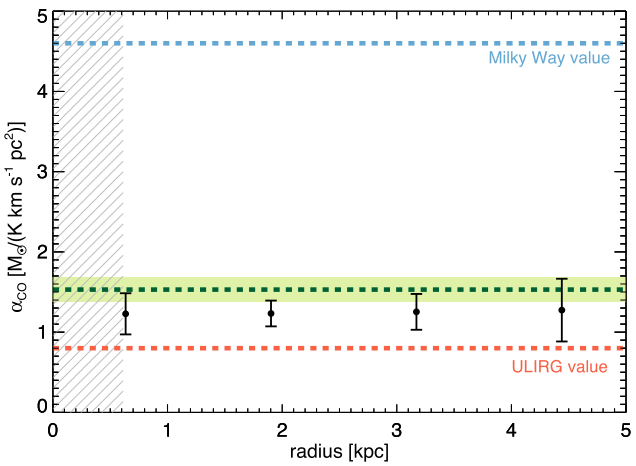

Figure A1. CO-to-H_2 conversion factor gradient across SHiZELS-19 from spatially resolved measurements and as a function of the galactocentric radius derived from the best-fitting kinematic model. The green-dashed line represents the galactic α_{CO} value derived from the tapered (2000 kλ) map and the green-shaded region shows the 1σ uncertainty. The blue- and red-dashed lines indicate the α_{CO} values usually adopted for the Milky Way and ULIRG like systems. The grey-dashed area represents the resolution element radial extent. We find a flat α_{CO} profile.

has a negative metallicity gradient (Molina et al. 2017) it does not vary enough in order to increase the α_{CO} value at larger radii.

We note that the α_{CO} radial profile values are slightly lower but still consistent within 1σ uncertainties with the galactic average CO-to-H_2 conversion factor value calculated from the tapered (2000 kλ) map. This is expected as the low spatial resolution data cube is able to trace CO(2–1) emission from the outskirts of the galaxy where the CO surface brightness is lower and the molecular gas has low metallicity compared to the inner parts. Both effects favour the increase of the average α_{CO} value.

It is worth to mention that by considering the large variety of metallicity gradients observed in high-redshift galaxies (e.g. Queyrel et al. 2012; Swinbank et al. 2012a; Molina et al. 2017), this result may be particularly applicable to SHiZELS-19 and it might not be used as typical property for the bulk population.

APPENDIX B: α_{CO} UPPER LIMIT FROM DYNAMICS

In Section 3.4 we have assumed the Narayanan et al. (2012)'s parametrization to estimate the CO-to-H_2 conversion factor. Using this α_{CO} value coupled with our dynamical mass calculus, we have constrained the dark matter content in the SHiZELS-19 galaxy. We have used the Narayanan et al. (2012)'s parametrization in detriment of Accurso et al. (2017)'s parametrization as the second is likely to be an upper limit for the CO-to-H_2 conversion factor as it does not consider the gas surface density effects (Bolatto et al. 2013). In order to confirm this assumption we use the dynamical mass calculus to constrain the CO-to-H_2 conversion factor (e.g. Tacconi et al. 2008).

We repeat the analysis done in Section 3.4, but now we calculate the total and stellar mass content within one CO half-light radius. The stellar mass within this radius is estimated by assuming an exponential stellar surface density profile, as suggested by the best-fitting Sérsic profile presented in Gillman et al. (2019) for the *HST*-F160W broad-band image. We caution, however, that this calculus also assumes a constant mass-to-light ratio across the SHiZELS-19 galactic disc. We calculate the thick-disc dynamical mass within one $r_{1/2,CO}$ by using the ∼kpc-scale kinematic CO observations (Fig. 3).

Initially we just constrain the α_{CO} lower limit value by imposing that the CO emission should be optically thick ($\alpha_{CO} \gtrsim 0.34$; Bolatto et al. 2013). We do not assume any dark matter content as we allow that the MCMC technique samples $\alpha_{CO} - f_{DM}$ phase space and fully considers the parameter degeneration introduced in equation (2).

In Fig. B1 we show the one- and two-dimensional posterior PDFs of the α_{CO} and f_{DM} parameters. As in Section 3.4, we find that higher α_{CO} values imply lower dark matter fractions. In the case of negligible central dark matter content within $r_{1/2,CO}$, we find an α_{CO} upper limit of 1.3(2.4) $M_\odot$ (K km s^{-1} pc^2)$^{-1}$ by considering 1(3) σ uncertainties.

This analysis suggests that the Accurso et al. (2017)'s parametrization overestimates the CO-to-H_2 conversion factor in SHiZELS-19 as this value is beyond the 3σ range derived from the α_{CO} PDF. Meanwhile, the CO-to-H_2 conversion factor estimated by assuming the Narayanan et al. (2012)'s parametrization is consistent within 1σ uncertainties. We note that an assumed $\alpha_{CO} \gtrsim 1$ implies that SHiZELS-19 may be baryon dominated ($f_{DM} < 0.5$) in its central zone, albeit dark matter dominated in its outskirts (Section 3.4; see also Tiley et al. 2019). This is consistent with the 'compaction' scenario (e.g. Dekel & Burkert 2014; Zolotov et al. 2015) in which the baryonic matter can cool and condense more efficiently than the collisionless dark matter, and thus, falling into the centre of the dark matter halo where they concentrate.

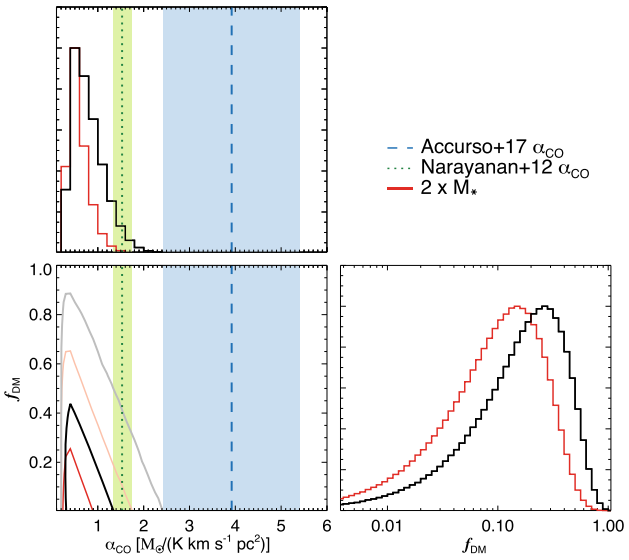

Figure B1. One- and two-dimensional posterior PDFs of the f_{DM} and α_{CO} parameters estimated by considering the total mass content within one CO half-light radius for SHiZELS-19. The data is colour coded in the same way as Fig. 6. This suggests an α_{CO} upper limit of 2.4 $M_\odot$ (K km s^{-1} pc^2)$^{-1}$ in the case of negligible dark matter content within this radius. This result rules out the Accurso et al. (2017)'s CO-to-H_2 conversion factor suggested for SHiZELS-19 by the 3σ.

This paper has been typeset from a TEX/LATEX file prepared by the author.